

Two-dimensional flows of foam: drag exerted on circular obstacles and dissipation

Benjamin Dollet^a Florence Elias^b Catherine Quilliet^a
Arnaud Huillier^a Miguel Aubouy^c François Graner^{a,*}

^a*Spectrométrie Physique, 140 rue de la Physique, BP 87, 38402 Saint Martin d'Hères Cedex, France*¹

^b*Laboratoire des Milieux Désordonnés et Hétérogènes, case 78, 4 place Jussieu, 75252 Paris Cedex 05, France*²

^c*SI3M, DRFMC, CEA, 38054 Grenoble Cedex 9, France*

Abstract

A Stokes experiment for foams is proposed. It consists in a two-dimensional flow of a foam, confined between a water subphase and a top plate, around a fixed circular obstacle. We present systematic measurements of the drag exerted by the flowing foam on the obstacle, *versus* various separately controlled parameters: flow rate, bubble volume, solution viscosity, obstacle size and boundary conditions. We separate the drag into two contributions, an elastic one (yield drag) at vanishing flow rate, and a fluid one (viscous coefficient) increasing with flow rate. We quantify the influence of each control parameter on the drag. The results exhibit in particular a power-law dependence of the drag as a function of the solution viscosity and the flow rate with two different exponents. Moreover, we show that the drag decreases with bubble size, increases with obstacle size, and that the effect of boundary conditions is small. Measurements of the streamwise pressure gradient, associated to the dissipation along the flow of foam, are also presented: they show no dependence on the presence of an obstacle, and pressure gradient depends on flow rate, bubble volume and solution viscosity with three independent power laws.

Key words: Foam, Stokes experiment, Drag, Dissipation

PACS: 82.70.Rr, 83.80.Iz, 47.50.+d, 47.60.+i

* Author for correspondence, fax +33 4 76 63 54 95, graner@ujf-grenoble.fr.

¹ UMR 5588 CNRS and Université Joseph Fourier.

² Fédération de Recherche FR 2438 "Matière et Systèmes Complexes", Paris, France.

1 Introduction

Liquid foams, like colloids, emulsions, polymer or surfactant solutions, are characterised by a complex mechanical behaviour. Those systems, known as soft complex systems, are multiphasic materials. Their constitutive entities are in interaction, generating internal structures, which cause the diversity in the fluid rheological behaviour [1]. Liquid foams are convenient model experimental system for studying the interplay between structure and rheology, since their internal structure can be easily visualised and manipulated.

Liquid foams are made of polyhedral gas bubbles separated by thin liquid boundaries forming a connected network. The liquid phase occupies a small fraction of the volume of the foam (several percent). The mechanics of liquid foams is rich: foams are elastic, plastic or viscous depending on the applied strain and strain rate [2]. This behaviour has been shown in rheological experiments performed on three-dimensional (3D) foams [3, 4, 5, 6]; models have been built to account for this diversity of rheological behaviour [7, 8, 9, 10]. However, the visualisation of the foam structure is technically difficult in 3D [11, 12], although progress have been made recently [13]. Moreover, the drainage of the liquid phase due to gravity may occur in 3D, making the fluid fraction and therefore the rheological moduli of the foam inhomogeneous [14]. An inhomogeneous liquid volume fraction of the foam may also cause an inhomogeneous coarsening of the foam, thus an inhomogeneous repartition of the bubble size.

For all these reasons, the mechanics of foams has been studied in two dimensions, where the direct visualisation of the structure is easier, and no gravity-driven drainage occurs if the system is horizontal. The system is then either a true 2D system like a Langmuir foam [15, 16], or quasi 2D system constituted by a monolayer of bubbles, either at the free surface of the solution (bubble raft [17, 18]), or confined between two horizontal transparent plates [19, 20], or between the surface of the solution and an upper horizontal transparent plate [21, 22]. The deformation and motion of individual cells have been forced and studied in different flow geometries: simple shear [17], flow in a constriction or around an obstacle [20], Couette flow [19, 18]. Some authors have been particularly interested in the dynamics of bubble rearrangements during the flow: the spatial distribution of the rearrangements [17, 19], the stress relaxation associated with the rearrangements [18], the deformation profile [23], the averaged velocity [19, 20]. However, no mechanical measurement has been performed in those last studies.

In this paper, we study the mechanics of a foam flowing in relative displacement with respect to an obstacle, at a constant velocity. In a Newtonian liquid at low Reynolds number, the force would vary linearly with the foam-obstacle

relative velocity, the proportionality factor being linked to the liquid viscosity and the size of the obstacle. This experiment gives then information on the effective viscosity of a flowing foam. Such a Stokes experiment has first been performed in a 3D coarsening foam by Cox et al. [24]. Here, the force exerted by the quasi 2D foam on the obstacle is measured, as a function of the flow velocity, in a 2D geometry. A similar experiment has been performed recently to investigate the elastic regime of a 2D foam and measure the foam shear modulus [16]. In the experiments presented here, the foam flows permanently around the obstacle, and the stationary regime is investigated. The system used is a monolayer of soap bubbles confined between the surface of the solution and a horizontal plate. This allows measuring accurately forces exerted on the obstacle and dissipation along the flow, and varying easily the foam internal parameters such as the viscosity of the solution, the bubble size, and the geometry of the obstacle.

The article is organised as follows. The experimental material and methods are presented in section II, the results are shown in section III for drag, and in section IV for dissipation. These results are discussed in section IV, and conclusions are exposed in section V.

2 Materials and methods

2.1 Foam production

The experimental setup is presented on Fig. 1(a). The experiments are performed in a glass channel of 110 cm length, 10 cm width and 10 cm depth. The soap solution is a solution of commercial dish-washing fluid (1% in volume) in purified water, with added glycerol when the viscosity needs to be varied (subsection 3.1). The surface tension of the solution is $\gamma = 31$ mN/m. At the beginning of each experiment, the channel is filled with the solution, with a 3.50 mm gap between the liquid surface and the coverslip. The foam is produced by blowing bubbles of nitrogen in the solution, at one end of the channel, in a chamber bounded by a barrier which allows a single monolayer of bubbles to form. The continuous gas flow makes the foam flow along the channel, between the surface of the solution and the coverslip. A typical image of the flowing foam observed from above is displayed in Fig. 2.

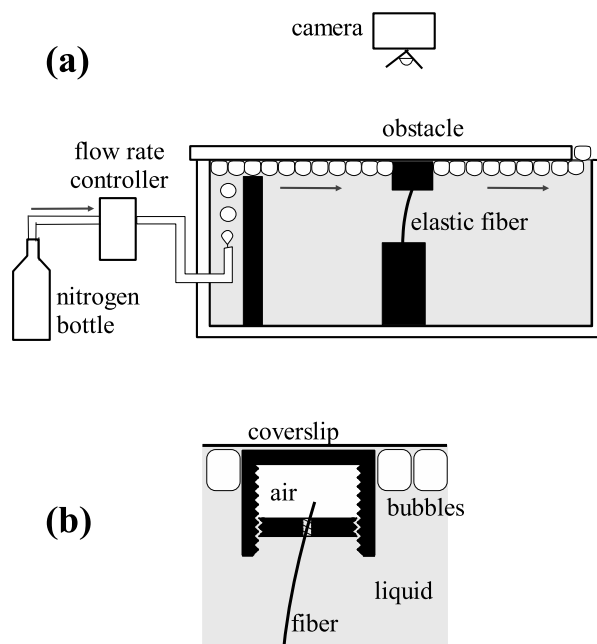


Fig. 1. (a) Experimental setup. The arrows indicate the flow of gas and foam. (b) Detailed sketch of the obstacle.

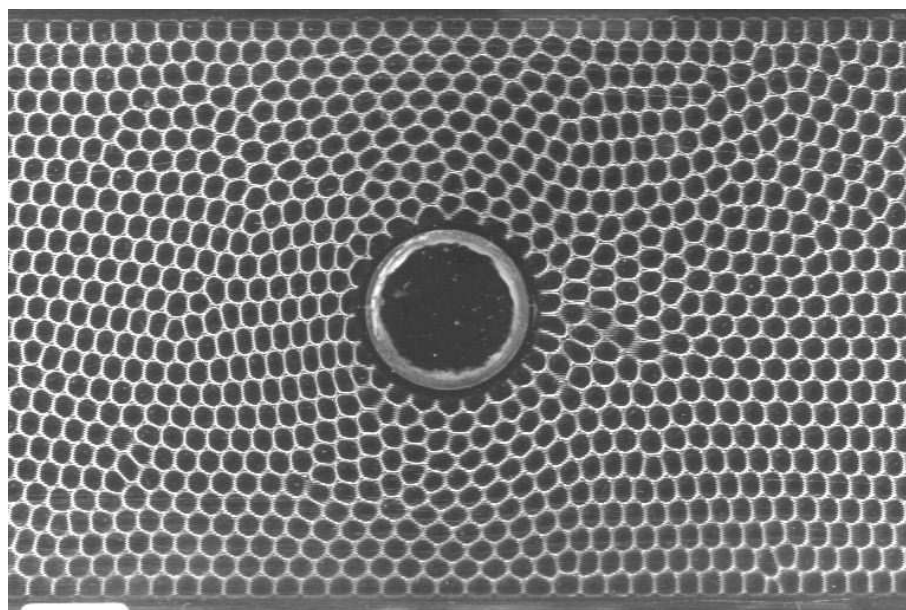


Fig. 2. Photo of foam flowing from left to right around a circular obstacle of diameter 30 mm. The bubble size is 16.0 mm^2 (note the monodispersity of the foam), and the flow rate is 174 mL/min. The walls of the channel (width 10 cm) are visible at the top and bottom of the picture. The stretching and shearing of bubbles due to the presence of the obstacle is clearly visible around the obstacle. The surface of the observed field is $15.4 \times 10.2 \text{ cm}^2$, and 1 pixel side equals 0.20 mm.

2.2 Obstacle and force measurements

The obstacle stands in the middle of the channel. It is a buoyant mobile plastic object connected to a fixed base by a soft glass fiber. The bottom extremity of the fiber is rigidly fixed. Its top extremity simply passes through a hole drilled in the bottom of the obstacle (Fig 1(b)). Therefore, the fiber can slide inside the horizontally moving obstacle, without applying any undesirable vertical force. Moreover, the fiber is lubricated by the liquid, which avoids solid friction against the obstacle.

The horizontal force F exerted by the foam on the obstacle tends to pull it streamwise; it is balanced by the horizontal drawback force F_d from the elastic fiber, whose deflection is designed by X . The calculation of this force is classical in the theory of elasticity; for a given displacement X from the position at rest of the mobile part, the drawback force writes [25]: $F_d = -KX$, where the rigidity K writes: $K = 3\pi ED^4/64L^3$, with $D = 240 \mu\text{m}$ the fiber diameter, L its vertical length and E its shear modulus. The fiber has been calibrated by measuring its deflection under its own weight, giving the value of the shear modulus : $E = 6.67 \times 10^{10}$ Pa. This value is compatible with typical values of the shear modulus of glass: $6-7 \times 10^{10}$ Pa. We use two different fibers, of vertical length $L = 34.8$ mm and $L = 42.4$ mm, depending on the magnitude of the force to measure. We have checked that for given experimental conditions, the same force is measured with both fibers (data not shown). The displacement is measured by tracking the position of the obstacle with a CCD camera placed above the channel: the actual position of the obstacle is given by the coordinates of its center, obtained by image analysis. The position of the center of the obstacle is known with a precision of 0.02 mm, much lower than the typical displacement (5 mm to 1 cm). When the obstacle has reached a stationary position under flow, the drawback force exactly compensates the force exerted by the foam, which is then directly deduced from the measured displacement.

The obstacle is in contact with the coverslip. This is necessary for the foam to flow around the obstacle and not above, but this may induce friction. Nevertheless, in the setup presented here, the obstacle is in contact with a single plate; this reduces the friction in comparison with an experiment performed in a Hele-Shaw cell, where the foam is confined between two plates. Furthermore, the obstacle is constituted by a hollow part closed by a watertight screw (Fig. 1(b)). It can thus enclose a tunable volume of air, which enables to tune its apparent density, chosen for the obstacle to float at the surface of the solution without applying an undesirable vertical force on the top plate. In the presence of the foam, the obstacle is in contact with the top plate through a capillary bridge, avoiding solid friction. We check for each experiment that the obstacle is not stuck: its position fluctuates under the slight flow hetero-

genities, and results presented below average the position of the obstacle over 50 successive images with an interval of two seconds. Viscous friction cannot be eliminated, but it only influences transients, which are not considered in this paper: each measurement is performed in a stationary regime. Reversibility and reproducibility tests give an upper bound for the force measurement errors: 0.2 mN, to be compared to the typical forces, of the order of 5 mN.

2.3 Dissipation measurements

The foam flowing in the channel experiences viscous friction, because of the velocity gradients between the bubbles, the coverslip and the subphase, and it exhibits energy dissipation through a pressure drop. If the channel remains horizontal, the thickness of the foam thus decreases along the channel, because its bottom is in contact with the subphase subject to hydrostatic pressure, and the foam can even run over the tank at its open end. We overcome this difficulty by tilting the whole setup thanks to a screw, so that the foam recovers constant thickness along the channel. Furthermore, the level difference h one has to impose between the two ends of the channel provides a simple measurement of the pressure drop ΔP of the foam through the hydrostatic pressure in the subphase: $\Delta P = \rho gh$, where ρ is the volumetric mass of the solution and $g = 9.8 \text{ m}\cdot\text{s}^{-2}$ the gravity acceleration. The thickness of the foam is measured at both ends of the channel by eye, thanks to a graduated rule placed on the side of the channel. When these measurements are done carefully, differences of thickness of $\Delta h = 0.1 \text{ mm}$ are detected. This yields a precision much better than the typical pressure drop, which correspond to level differences of order 2 to 15 mm.

We have checked that when the thickness of the foam is equal at both ends, it also remains constant along the channel, which means that the rate of dissipation per unit length is also constant. Instead of the pressure drop ΔP , we will therefore deal with the pressure gradient $\nabla P = \Delta P/L$, where $L = 110 \text{ cm}$ is the length of the channel. We have also checked that the pressure gradient does not depend on the presence of the obstacle, measuring the same pressure drop with the three different obstacles studied in this paper and without obstacle (data not shown). This enables to consider the pressure gradient as the relevant parameter to quantify the dissipation of the foam flowing in the channel.

2.4 Control parameters

A first control parameter is the nitrogen flow rate Q , which is adjusted using an electronic controller (Brooks Instrument B.V.) driven by a home-made

software. The range of available flow rate runs on more than three decades, from 1 to 2,000 mL/min, with a precision of 0.1 mL/min. Another control parameter is the bubble volume. It is indirectly determined by measuring the surface density of bubbles against the coverslip thanks to image analysis, using NIH Image software. Since the foam thickness is kept equal to the initial 3.50 mm gap between the surface of the solution and the coverslip, there is a univoque relation between the bubble volume and the mean surface density. Instead of this surface density, we will refer throughout this paper to its invert, that we call bubble area. This parameter differs slightly from the bubble area one can measure directly on an image, because it includes the water contained in the films and Plateau borders surrounding bubbles. For a given injector, the bubble volume increases with the gas flow rate. To control these two parameters separately, we blow the gas through one to six tubes (or needles) of same diameter simultaneously, keeping constant the flow rate per tube, hence the bubble volume. Furthermore, the diameter of these injectors can be varied, which changes the flow rate per tube for the same bubble area; hence, for a given bubble volume, typically ten different values of flow rate are allowed. We always produce monodisperse foams: the bubble area disorder, measured as the ratio of the standard deviation with the mean value of the bubble area distribution, is less than 5%. Six different bubble areas were used: 12.1, 16.0, 20.0, 25.7, 31.7 and 39.3 mm², with a relative precision of 3%. The study of smaller bubbles would be problematic, since a transition from bubble monolayer to multilayer occurs at low horizontal area/height ratio [26]. At the other extremity, it would be difficult to make a monodisperse foam with larger bubbles.

Another tunable parameter is the viscosity of the solution. We control it by adding glycerol to the initial soap solution. We have used five different solutions, with 0, 20, 30, 40 and 50% glycerol in mass. The respective kinematic viscosities ν , measured with a capillary viscometer (Schott-Geräte) at room temperature, are equal to 1.06, 1.6, 2.3, 3.8 and 9.3 mm²/s. The variation of viscosity due to the variation of room temperature is lower than 4%.

Different obstacles have been used. The basic obstacle, whose density is tunable, is a cylinder of diameter 30 mm on which additional profiles can be fixed. We have studied three different obstacles: two cylinders, of diameter 30 and 48 mm, and a cogwheel of diameter 43.5 mm, with circular cogs of diameter 4 mm (Fig. 3). For each obstacle, the apparent density is adjusted as described above to avoid solid friction. As said previously, the presence of the obstacle influences the measurements of drag, but not those of dissipation.

As a final remark about control parameters, for given solution viscosity, area and obstacle, various flow rates are available (from 5 to 13 in the following data), with greatest flow rate at least 20 times greater than the lowest one.

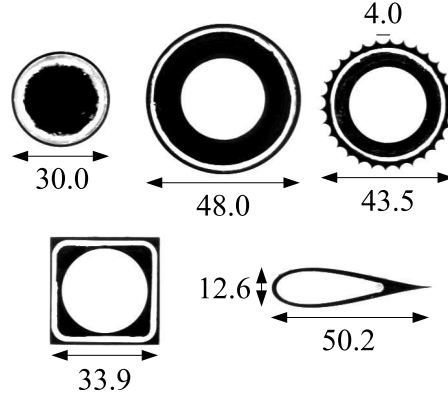


Fig. 3. Top views of the three obstacles.

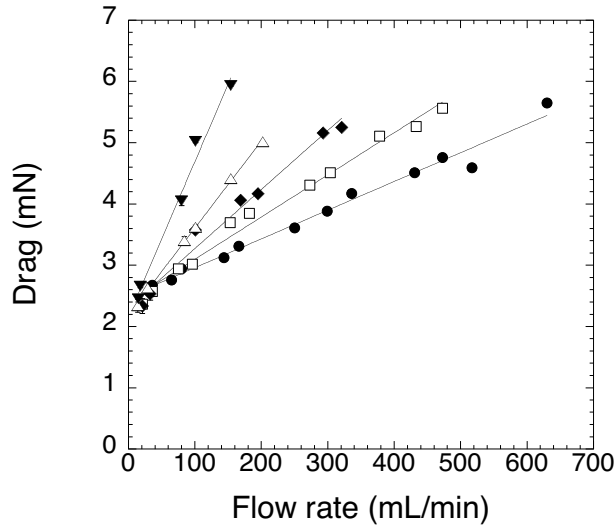


Fig. 4. Drag *versus* flow rate, for solution viscosity equal to 1.06 (●), 1.6 (□), 2.3 (◆), 3.8 (△) and 9.3 mm²/s (▼). The straight lines are linear fits of the data. The bubble area is 20 mm² and the obstacle is a circle of diameter 30 mm.

3 Drag measurements

3.1 Influence of solution viscosity

We study the variation of the drag *versus* the flow rate and the solution viscosity, for the five different viscosities indicated in subsection 2.4. All these measurements are performed at a fixed bubble area of 20 mm², and we use a circular obstacle of diameter 30 mm.

We observe two general features (Fig. 4), independent of the value of the solution viscosity: the drag does not tend to zero at low flow rate, and it increases with flow rate. The first observation is a signature of the solid-like properties of the foam. The second feature is related to the fluid-like properties

of the foam. The data are well fitted by a linear law (Fig. 5):

$$F = F_0 + mQ. \quad (1)$$

We call F_0 the yield drag, as a reference to the yield properties of the foam, and the slope m the viscous coefficient, since we can dimensionally deduce from m an effective viscosity μ for the foam: $\mu \approx mS/R$, where S is the cross-section of the foam, and R is the typical size of the obstacle. Yield drag *versus* solution viscosity is plot on Fig. 5(a), and viscous coefficient *versus* solution viscosity on Fig. 5(b).

Fig. 5(a) shows that the yield drag is essentially independant of the solution viscosity. This was expected, because yield drag is only related to the yield properties of the foam, which depend on surface tension and bubble size [27]. The slight decrease with the solution viscosity is likely due to a slight decrease of surface tension with the glycerol rate in the solution, as quantified for aqueous mixtures of glycerol without surfactant, whose surface tension decreases by 7% from pure water to a mixture with half glycerol in mass [28].

Fig. 5(b) shows that the viscous coefficient increases with the solution viscosity. The data can be fitted by a power law (insert of Fig. 5(b)), that yields the following dependency of viscous coefficient on solution viscosity: $m \propto \nu^{0.77 \pm 0.05}$.

3.2 Influence of bubble area

We now turn to the study of drag versus flow rate and bubble area. All the measurements are done without adding glycerol in the solution, at a constant viscosity of 1.06 mm²/s. The obstacle is a cylinder of radius 30 mm. We study the six bubble areas indicated in subsection 2.4, from 12.1 mm² to 39.3 mm².

We find again the signature of the viscoplastic properties of the foam (Fig. 6), with a non-zero yield drag and an increase of drag *versus* flow rate. Performing the linear fit (1), we get the yield drag and the viscous coefficient, plotted *versus* bubble area in Fig. 7.

Fig. 7(a) evidences that the yield drag is a decreasing function of the bubble area. This is coherent with the fact that both quantities used to describe the solid properties of the foam, its shear modulus and yield stress, are also decreasing functions of the bubble size [29, 3, 4]. Fig. 7(b) shows that the viscous coefficient is also a decreasing function of bubble area, except for the last point. Further analysis of these data is somewhat complex, and will be discussed in more detail in subsection 5.2.

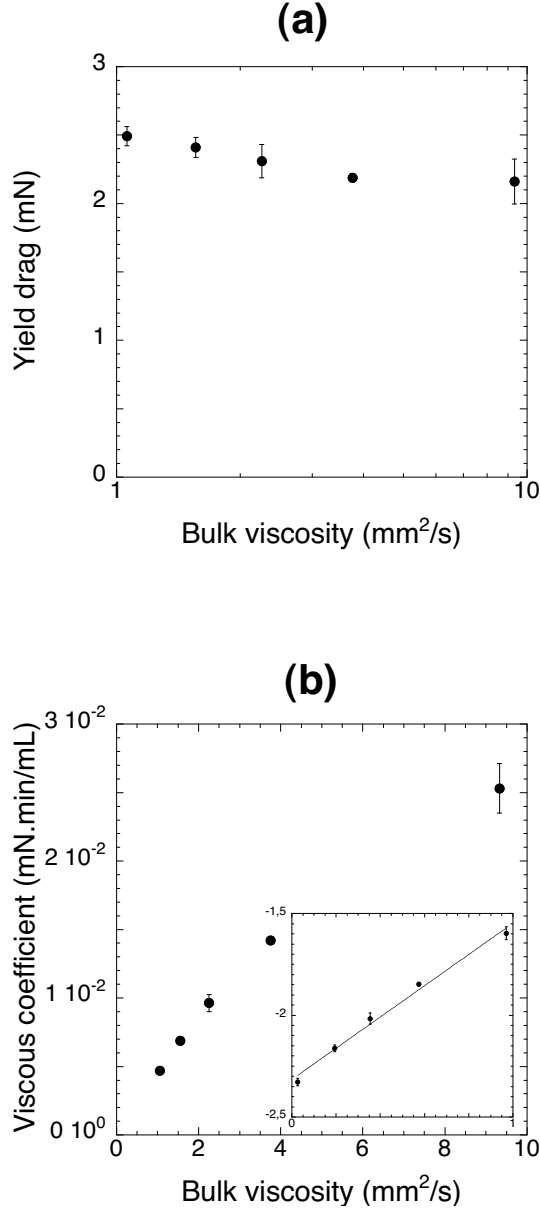


Fig. 5. Results from fits to Fig. 4. (a) Yield drag *versus* the solution viscosity (semi-logarithmic scale), and (b) viscous coefficient *versus* the solution viscosity (linear scale). Insert: log-log plot. The straight line is the linear fit: its slope is 0.77 ± 0.05 .

3.3 Influence of obstacle size and boundary conditions

We now study a third control parameter: the obstacle geometry. As indicated in subsection 2.4, we use two cylinders of different radius and a cogwheel. This enables to study the influence of the size of the obstacle and of the boundary conditions: the foam slips along the smooth cylinders whereas the first layer of bubbles around the cogwheel is anchored in the cogs. As in the previous

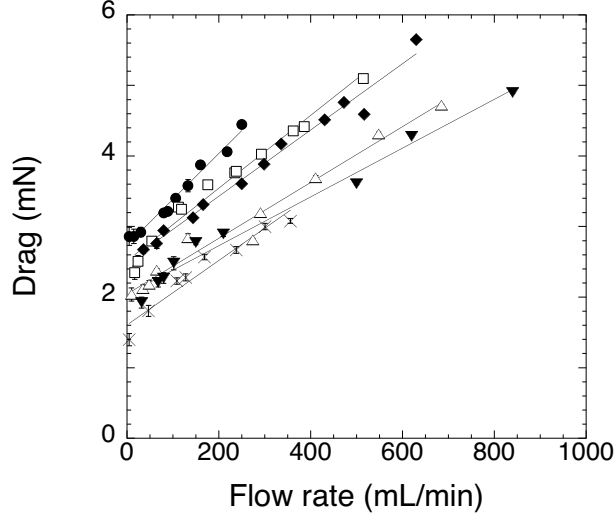


Fig. 6. Drag *versus* flow rate, for bubble area equal to 12.1 (\bullet), 16.0 (\square), 20.0 (\blacklozenge), 25.7 (\triangle), 31.7 (\blacktriangledown) and 39.3 mm² (\times). The straight lines are linear fits of the data. The solution viscosity is 1.06 mm²/s and the obstacle is a circle of diameter 30 mm.

subsection, the solution of viscosity of 1.06 mm²/s is used. A bubble area of 16.0 mm² was chosen in order to adapt the bubble size to the cog diameter, for the bubbles to be correctly trapped in the cogs.

As expected, the drag increases with the size of the obstacle (Fig. 8). The results of the linear fit (1) are displayed in Fig. 9(a) and 9(b) *versus* obstacle diameter. There are three possible choices for the cogwheel diameter: a mean diameter of 43.5 mm, which would be the diameter of the obstacle without cogs, an inner diameter of 39.5 mm if the cogs are excluded, and an outer diameter of 47.5 mm if the bubbles trapped in cogs are included. Hence, three points are represented for inner, mean and outer diameter of the cogwheel in Fig. 9.

Fig. 3 shows that the increase of drag with obstacle diameter is close to linear, and we fit the data by a linear law passing through zero. This is a way to study the influence of boundary conditions, since it enables to consider the cogwheel as an effective obstacle, whose effective diameter is given by the fitting line for the values of yield drag and viscous coefficient of the cogwheel. This effective diameter is to compare to the three possible choices described above for the diameter of the cogwheel. Concerning the yield drag, Fig. 9(a) shows that the effective diameter is close to the outer one, whereas for the viscous coefficient, Fig. 9(b) shows that it is close to the inner one. This difference between the behaviour of the cogwheel for yield drag and viscous coefficient is discussed in the next section.

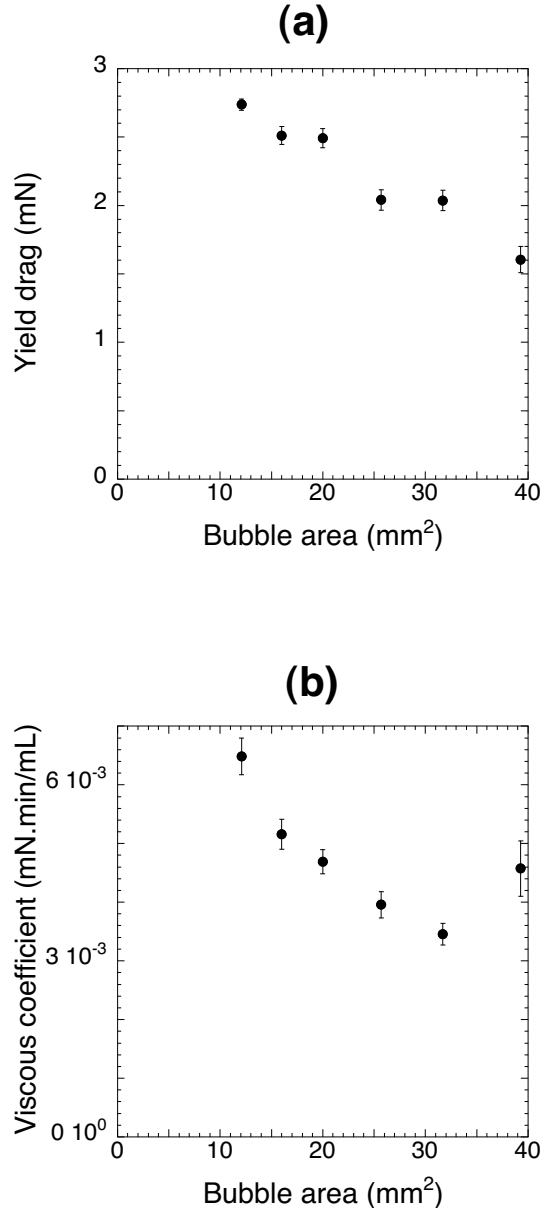


Fig. 7. Results from fits to Fig. 6. (a) Yield drag, (b) viscous coefficient *versus* bubble area.

4 Dissipation measurements

For each experiment, the drag and the pressure gradient are simultaneously and independently measured. We thus present systematic measurements for the pressure gradient like for the drag, studying the same control parameters except the obstacle, whose presence do not change the results, as mentioned above.

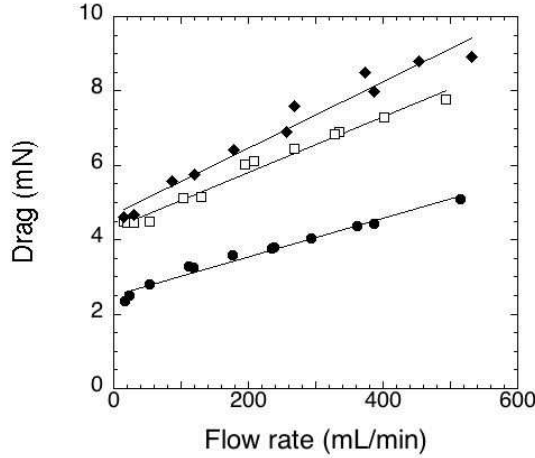


Fig. 8. Drag *versus* flow rate, for the following obstacles: cylinder of diameter 30 mm (●), cogwheel of diameter 43.5 mm with cylindrical teeth of diameter 4 mm (□), and cylinder of diameter 48 mm (◆).

4.1 Influence of solution viscosity

We study the variation of the pressure gradient *versus* the flow rate and the solution viscosity, for the five different viscosities indicated in subsection 2.4. All these measurements are performed at a fixed bubble area of 20 mm².

We observe that the pressure gradient increases with both the flow rate and the solution viscosity (Fig. 10(a)). These tendencies are quantified by the log-log plot (Fig. 10(b)). For each solution viscosity, the data are well linearly fitted, indicating that the pressure gradient depends on the flow rate with a power-law dependence. Furthermore, all fitting lines are nearly parallel; this exponent is thus independent of the solution viscosity, and its value obtained by averaging over the five solution viscosities equals 0.62 ± 0.03 . To quantify the dependency of the pressure gradient on the solution viscosity, we thus use the following fit: $\log \nabla P = 0.62 \log Q + m_2$, and plot the coefficient m_2 , as a function of the logarithm of the solution viscosity in Fig. 11. The data are again well fitted by a linear law, indicating another power-law dependence of the pressure gradient, on the solution viscosity, with an exponent equal to 0.41 ± 0.04 .

4.2 Influence of bubble area

We now present the study of pressure gradient versus flow rate and bubble area. All the measurements are done without adding glycerol in the solution,

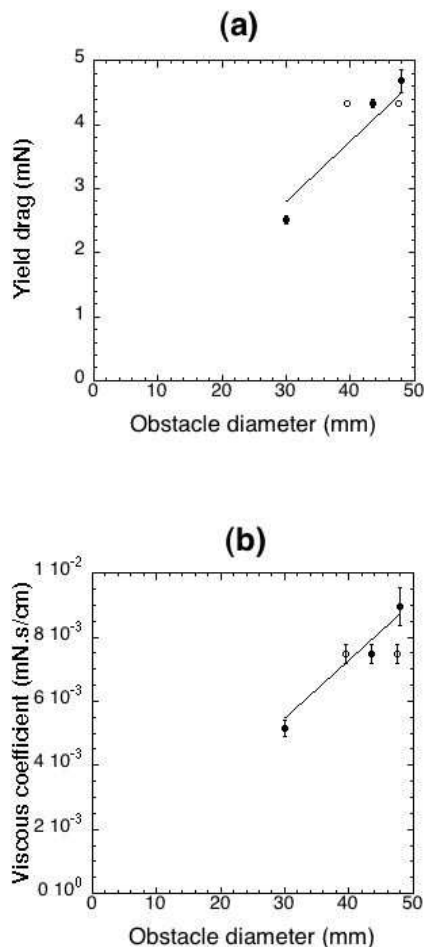


Fig. 9. (a) Yield drag, and (b) viscous coefficient *versus* the obstacle diameter. The cogwheel is represented by three points, which correspond to the three possible choices for its diameter: inner diameter of 39.5 mm (left \circ), mean diameter of 43.5 mm (\bullet), and outer diameter of 47.5 mm (right \circ). The straight line is a linear fit to the two cylinders data passing through zero.

at a constant viscosity of $1.06 \text{ mm}^2/\text{s}$. We study the six bubble areas indicated in subsection 2.4.

We observe that the pressure gradient increases again with the flow rate, and decreases with the bubble area (Fig. 12(a)). The log-log plot is displayed in Fig. 12(b). The relative variation of bubble area is smaller than the one of solution viscosity, but for each bubble area, the data are again well linearly fitted with fitting lines nearly parallel, yielding an exponent of 0.58 ± 0.04 for the power-law dependance of the pressure gradient on the flow rate. This exponent is compatible with the one obtained in the previous subsection, to within the experimental errors. To quantify the dependency of the pressure

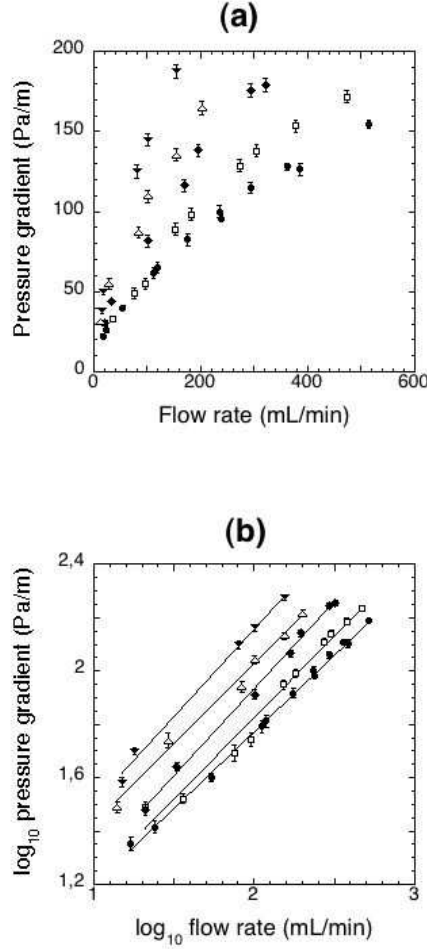


Fig. 10. (a) Pressure gradient *versus* flow rate, for solution viscosity equal to 1.06 (\bullet), 1.6 (\square), 2.3 (\blacklozenge), 3.8 (\triangle) and 9.3 $\text{mm}^2\cdot\text{s}^{-1}$ (\blacktriangledown). (b) Log-log plot of the same data.

gradient on the bubble area, we use the fit: $\log \nabla P = 0.58 \log Q + m_2$, and plot the coefficient m_2 , as a function of the logarithm of the bubble area in Fig. 11. The data are remarkably linearly fitted, indicating a third power-law dependence of the pressure gradient, on the bubble area, with an exponent equal to -0.33 ± 0.01 .

To conclude this section about the dissipation measurements, we have shown that the pressure gradient has a power-law dependance on the three studied control parameters: flow rate, solution viscosity and bubble area, with three independent exponents: $\nabla P \propto Q^\alpha \nu^\beta A^\delta$. However, the values we got for β and δ depended on two different chosen values for α , respectively 0.62 and 0.58, and they are therefore biased. Unbiased values are obtained by direct fit of the whole data (89 independent experiments) by the triple power-law above,

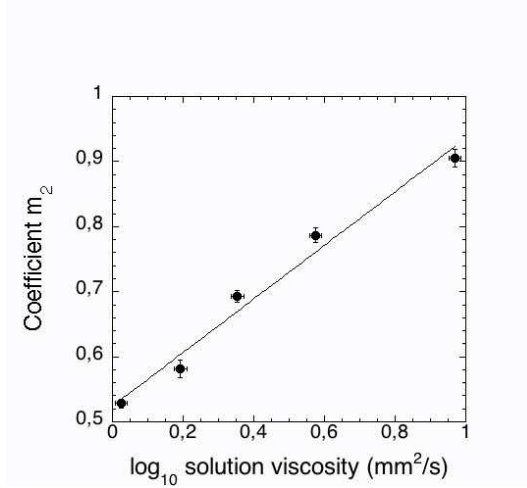


Fig. 11. Coefficient m_2 of the fit $\log \nabla P = 0.62 \log Q + m_2$ versus the logarithm of the solution viscosity. The straight line is a linear fit of the data.

and we finally get the following scaling for the pressure gradient:

$$\nabla P(\text{Pa/m}) = (10.0 \pm 0.4) \left(\frac{Q}{Q_0} \right)^{0.59 \pm 0.01} \left(\frac{\nu}{\nu_0} \right)^{0.46 \pm 0.02} \left(\frac{A}{A_0} \right)^{-0.34 \pm 0.03},$$

where $Q_0 = 1 \text{ mL/min}$, $\nu_0 = 1 \text{ mm}^2/\text{s}$ and $A_0 = 1 \text{ mm}^2$. Note that as expected, the precision of the exponent is better for parameters running on a wider range.

5 Discussion

5.1 Influence of solution viscosity

Our measurements of drag and pressure gradient versus viscosity ν and flow rate Q yield the following scalings:

$$F(Q, \nu) = F_0 + \text{const} \times \nu^{0.77 \pm 0.05} Q, \quad (2)$$

and:

$$\nabla P(Q, \nu) = \text{const} \times \nu^{0.46 \pm 0.02} Q^{0.59 \pm 0.01}. \quad (3)$$

(see subsection 3.1 and section 4). To our knowledge, this is the first time than such scalings are proposed to quantify the dynamical regime of flowing foams in channels. Up to now, the dynamic regime of flowing foam has been mainly investigated through the study of pressure drop of foam confined

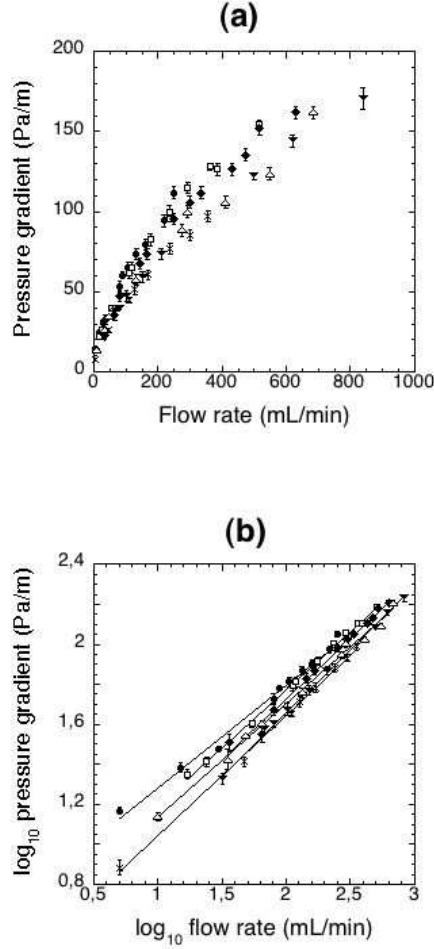


Fig. 12. (a) Pressure gradient *versus* flow rate, for bubble area equal to 12.1 (\bullet), 16.0 (\square), 20.0 (\blacklozenge), 25.7 (\triangle), 31.7 (\blacktriangledown) and 39.3 mm² (\times). (b) Log-log plot of the same data.

in capillaries (see Cantat et al. [30] and references therein). Since the early work of Bretherton [31], who studied the friction between an infinitely long bubble and a solid wall, all these studies emphasize the role of the capillary number $Ca = \eta V / \gamma$, where η is the dynamic viscosity of the solution, γ its surface tension and V the velocity of the flowing foam. In the frame of our study, the capillary number is proportional to the product νQ . It appears from our scalings (2) and (3) that such a number is not sufficient to describe the dynamic regime of a flowing foam, because the exponents for viscosity and flow rate differ significantly. Bretherton's theory is therefore not sufficient to explain our measurements: additional physical ingredients are involved, like detailed bubble shape and interfacial rheology (surface elasticity and viscosity). This has not been investigated yet. However, it is worth noting that from the scalings (2) and (3), the quantity $[F(Q, \nu) - F_0]^{0.59} / \nabla P(Q, \nu)$ does not

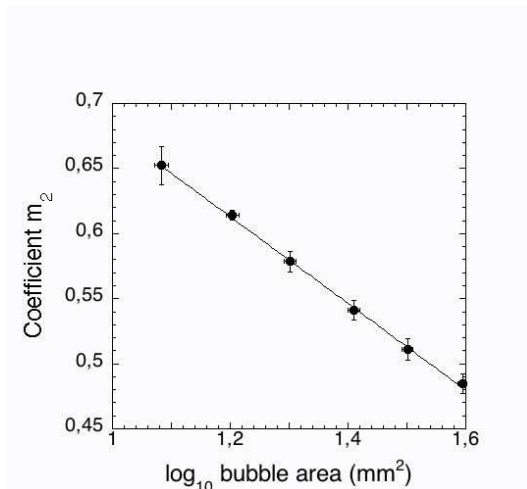


Fig. 13. Coefficient m_2 of the fit $\log \nabla P = 0.58 \log Q + m_2$ versus the logarithm of the bubble area. The straight line is a linear fit of the data.

significantly depend neither on flow rate, nor on solution viscosity. This confirms that both the dissipation and the velocity-dependent part of the drag are generated by a common mechanism, the viscous friction between bubbles and solid boundaries.

Furthermore, the scaling (3) shows that the exponent of the pressure gradient significantly departs from $2/3$, which is the exponent expected for tangentially perfectly mobile interfaces (implicit assumption in Bretherton's theory [31]), as well as from $1/2$, predicted value for rigid interfaces [32]. This probably means that with the used surfactants, the behaviour of the interfaces lies between these two extreme cases.

5.2 Influence of bubble area

The measurements of drag versus bubble area and flow rate, in subsection 3.2, show that both yield drag and viscous coefficient are decreasing functions of the bubble area. This is expected for the yield drag, since the foam shear modulus and yield stress are decreasing functions of the bubble size [29, 3, 4]. However, the yield stress of the foam is not the only contribution to the yield drag, and preliminary simulations of our experiments [35] show that the resultant of the pressure of bubbles in contact with the obstacle is a second non-negligible contribution to the yield drag, and that these two contributions act in the same sense. Since we are not able to measure the pressure in the bubbles, we cannot quantify the pressure contribution in our experiments, so the interpretation of the evolution of yield drag versus bubble area (Fig. 7(a)) is difficult and requires further numerical simulations.

Another major difficulty for quantitative interpretation arises from the variation of fluid fraction with bubble area. In our setup, the monolayer of bubbles is in contact with a reservoir of water, and the amount of water in the Plateau borders and films between bubbles is freely chosen by the system. For instance, we have observed that little bubbles are more closely packed than big ones. Therefore, the mean fluid fraction should vary with bubble area. Furthermore, local effects such as dilatancy [36] could increase the fluid fraction near the obstacle, because of the shear experienced by the foam in this zone. This complicates the interpretation of the evolution of yield drag with bubble area, because many studies have shown that rheological properties of foams and emulsions strongly depend on fluid fraction [3, 4, 6].

Despite the complications due to the effect of fluid fraction, we can propose a qualitative argument to explain why the viscous coefficient decreases with the bubble area, based on the dissipation model of Cantat and coworkers [30]. These authors state that dissipation in flowing foam is localised in the Plateau borders between bubbles and walls. Hence, dissipation should increase with the number of bubbles surrounding the obstacle, and therefore the viscous coefficient should decrease with the bubble area, which is actually seen in Fig. 7(b). The scaling of the pressure gradient with the bubble area, $\nabla P \propto A^{-0.34 \pm 0.03}$ (see section 4), is also compatible with this model. However, we should expect the pressure gradient to be proportional to the total length of the Plateau borders per unit area of foam. Since the foams are monodisperse in our experiments, we should thus expect a scaling $\nabla P \propto 1/\sqrt{A}$, which differs from ours. Actually, this scaling applies for sharp Plateau borders, matching a flat thin film between a bubble and a wall and another one between two bubbles. Such an idealisation does not apply to our experiments, since the bubble shape is essentially curved, hence Plateau borders are much smoother. Furthermore, the shape of the bubbles strongly depends on their volume, because of the influence of buoyancy. Note also that this model does not capture the increase of viscous coefficient observed for the bubble area of 39.3 mm².

As an additional remark, friction in the foam should strongly depend on the boundary conditions at the interfaces between films and bubbles, hence the viscous coefficient probably changes with the surface rheology. It would thus be interesting to investigate the influence of the surfactant used on the drag measurements.

5.3 *Influence of the obstacle geometry*

The measurements of drag for different obstacles, presented in subsection 3.3, show that both the yield drag and the viscous coefficient increase linearly with

the diameter of the obstacle, and that the effect of the boundary conditions on the obstacle is not marked. We now discuss these two observations.

Our measurements of drag around circular obstacles are to compare to the theoretical value of the drag exerted by a Newtonian fluid of dynamic viscosity η , flowing at velocity V , on a cylindrical obstacle of radius R in a channel of width $2H$ [37]:

$$F \simeq \frac{4\pi\eta RV}{\ln H/R - 0.91}. \quad (4)$$

It is worth noting that this law does not predict proportionality between the drag and the obstacle diameter when R/H ranges from 0.3 to 0.5, contrary to our observations. This indicates again that the elastic properties of the foam are significant, even when we consider only the evolution of viscous coefficient *versus* obstacle diameter (Fig. 9(b)). This is to compare to the simulations of Mitsoulis and coworkers [33, 34], who computed the drag exerted by a flowing Bingham plastic on a cylinder in the same geometry than ours, for different values of obstacle diameters. A Bingham plastic is characterized by its yield stress τ_y and its plastic viscosity μ , and it follows the constitutive equation: $\tau = \tau_y + \mu\dot{\gamma}$ for $|\tau| > \tau_y$, and $\dot{\gamma} = 0$ for $|\tau| < \tau_y$, where τ is the shear stress and $\dot{\gamma}$ the applied strain. To summarize, Mitsoulis and coworkers show that the drag exerted by a flowing Bingham plastic around a cylinder strongly depends on the Bingham number $\text{Bn} = 2R\tau_y/\eta V$ comparing elastic and viscous contribution: at a given Bingham number of order unity, there is a crossover between a Newtonian-like behaviour of the drag (for $\text{Bn} \ll 1$) given by formula (4), and an elastic-like (for $\text{Bn} \gg 1$) where drag does not significantly depend on the velocity and is roughly proportional to the cylinder diameter. Though modeling foam as a Bingham plastic is an open debate, this work provides an interesting comparison to our experimental measurements, for which we now evaluate the order of magnitude of the Bingham number in our experiments. The yield stress for a foam is of order [27] $0.5\gamma/a$, with $\gamma = 31$ mN/m the surface tension and $a \approx \sqrt{16/(3^{3/2}/2)} \approx 2.5$ mm the typical length of a bubble edge (we recall that the bubble area is 16.0 mm² in the considered experiments, and compute a for an hexagonal bubble), so $\tau_y \approx 6$ Pa (to be rigorous, this overestimates the yield stress for a wet foam). Furthermore, we can deduce from the value of the viscous coefficient ($m = 5 \times 10^{-6}$ N·min/mL after Fig. 7(b)) a rough value of the plastic viscosity of the foam: dimensional analysis yields $\mu \approx mS/R$ where S is the cross-section of the foam, so Bingham number writes $\text{Bn} \approx 2R^2\tau_y/mQ$. The typical value of flow rate in our experiments is 10^2 mL/min, hence the typical Bingham number equals $\text{Bn} \approx (2 \times 0.015^2 \times 6)/(5 \times 10^{-6} \times 10^2) \approx 5$. Though this is a very rough evaluation of the Bingham number, this tends to confirm that in our range of flow rates, this parameter remains of order unity, hence both

elastic and fluid properties of the foam are involved in the interaction with the obstacle to create the drag.

We have observed in subsection 3.3 that the effective diameter of the cogwheel is different if we consider the yield drag or the viscous coefficient. For the yield drag, the cogwheel behaves like a large cylinder, thus including the trapped bubbles. On the other hand, for the viscous coefficient, the cogwheel behaves like a smaller cylinder. Actually, the cogwheel and the trapped bubbles form a closed system during the experiment: no rearrangement of the trapped bubbles occurs after all the teeth have been filled with bubbles. So this system behaves as an effective obstacle, but with an external boundary constituted of bubble edges, instead of a solid boundary. This explains the difference observed between the yield drag and the viscous coefficient: at low velocity, the foam feels the presence of the effective obstacle, but at high velocity, the friction between the effective obstacle and the surrounding flowing bubbles is lower than the friction between a solid obstacle and its neighbouring flowing bubbles. To be more quantitative, it would be interesting to study the influence of interfacial rheology on this friction. Anyway, the measurements show that the influence of boundary conditions is not dramatic, probably because it does not change much the features of the flow beyond the first layer of bubbles.

6 Conclusions

This work provides the first detailed and systematic measurements of the force exerted by a 2D flowing foam on an obstacle as a function of various control parameters: flow rate, solution viscosity, bubble volume and obstacle shape and size. All the data show two contributions to the drag: a yield drag for flow rate tending to zero, and a flow rate-dependant contribution. We have shown that the yield drag is independent of the solution viscosity, decreases with bubble volume and linearly increases with the obstacle diameter. Fitting the flow rate-dependant contribution by a linear law, we have shown that the slope (or viscous coefficient) increases with the solution viscosity as a power law with an exponent of 0.77 ± 0.05 ; moreover, the viscous coefficient globally decreases with the bubble volume and linearly increases with the obstacle diameter. Furthermore, we have pointed out that the effect of boundary conditions on the obstacle is not striking.

This paper also presents a systematic study of the dissipation of a 2D flowing foam in a channel as a function of the same control parameters that for the drag. Dissipation is quantified by a pressure gradient, which is independent of the presence of an obstacle, and scales with the three parameters with a power-law dependence: the exponents equal 0.59 ± 0.01 for the flow rate, 0.46 ± 0.02 for the solution viscosity, and -0.34 ± 0.03 for the bubble area.

Though this scaling is quite accurate, it remains difficult to interpret, both because of the complex bubble geometry and because the interfacial rheology is not well characterised with the used surfactant.

This work opens many perspectives. Other control parameters remain to be studied, like polydispersity and rheological properties of the surfactants. The effects of those parameters on the drag could help to study their influence on foam rheology, and to explain the scaling of the pressure gradient. Furthermore, the use of asymmetric obstacles such as airfoil profiles will enlarge the range of studied effects, allowing lift, torque or orientation under flow. Pressure drop measurements, allowing to study dissipation in foams [30], are also currently investigated by the authors. Now, a local analysis of the local stresses, deformations [38] and velocity fields is required to provide a more detailed comprehension of the foam rheology. The comparison between this local analysis and the global properties of the foam, such as our drag measurements, could provide a way to propose and test constitutive equations for the mechanics of foams.

Acknowledgements

The authors would like to thank Franck Bernard, Kamal Gam and Julien Deffayet for experimental help, the machine shop of Laboratoire de Spectrométrie Physique and Patrice Ballet for technical support, and Simon Cox, Wiebke Drenckhan, Isabelle Cantat and Renaud Delannay for enlightening discussions.

References

- [1] R. G. Larson, *The Structure and Rheology of Complex Fluids*, Oxford University Press, New York (1999).
- [2] D. Weaire, S. Hutzler, *The physics of foams*, Oxford University Press, Oxford (1999).
- [3] T. G. Mason, J. Bibette, D. A. Weitz, *Phys. Rev. Lett.* **75**, 2051 (1995).
- [4] T. G. Mason, J. Bibette, D. A. Weitz, *J. Coll. Int. Sci.* **179**, 439 (1996).
- [5] S. Cohen-Addad, H. Hoballah, R. Höhler, *Phys. Rev. E* **57**, 6897 (1998).
- [6] A. Saint-Jalmes, D. J. Durian, *J. Rheol.* **43**, 1411 (1999).
- [7] D. A. Reinelt, A. Kraynik, *J. Rheol.* **44**, 453 (2000).
- [8] P. Sollich, F. Lequeux, P. Hébraud, M. E. Cates, *Phys. Rev. Lett.* **78**, 2020 (1997).
- [9] D. J. Durian, *Phys. Rev. Lett.* **75**, 4780 (1995).
- [10] M. E. Cates, P. Sollich, *J. Rheol.* **48**, 193 (2004).

- [11] C. Monnereau, M. Vignes-Adler, in *Foams and Emulsions*, Ed. J.F. Sadoc and N. Rivier, NATO ASI Series E: Applied Sciences, **354**, Kluwer, 359 (1999).
- [12] B. Prause, J. A. Glazier, S. Gravina, C. Montemagno, *J. Phys.: Cond. Matt.* **7**, L511 (1995).
- [13] J. Lambert, I. Cantat, R. Delannay, G. Le Caër, A. Renault, S. Ruellan, F. Graner, S. Jurine, P. Cloetens, J. A. Glazier, proceedings of Eufoam 2004, to appear in *Coll. Surf. A* (2004).
- [14] S. A. Koehler, S. Hilgenfeldt, H. A. Stone, *Europhys. Lett.* **54**, 335 (2001).
- [15] M. Lösche, E. Sackmann, H. Möhwald, *Ber. Bunsenges. Phys. Chem.* **87**, 2506 (1983).
- [16] S. Courty, B. Dollet, F. Elias, P. Heinig, F. Graner, *Europhys. Lett.* **64**, 709 (2003).
- [17] A. Abd el Kader, J. J. Earnshaw, *Phys. Rev. Lett.* **82**, 2610 (1998).
- [18] E. Pratt, M. Dennin, *Phys. Rev. E* **67**, 051402 (2003).
- [19] G. Debrégeas, H. Tabuteau, J.-M. Di Meglio, *Phys. Rev. Lett.* **87**, 17-8305 (2001).
- [20] M. Asipauskas, M. Aubouy, J. A. Glazier, F. Graner, Y. Jiang, *Granular Matt.* **5**, 71 (2003).
- [21] C. S. Smith, in *Metal Interfaces*, American Society for Metals, Cleveland, Ohio, 65 (1952).
- [22] M. F. Vaz, M. A. Fortes, *J. Phys.: Cond. Matt.* **9**, 8921 (1997).
- [23] E. Janiaud, F. Graner, cond-mat/0306590, submitted to *J. Fluid Mech.*
- [24] S. J. Cox, M. D. Alonso, S. Hutzler, D. Weaire, in *Proceedings of the 3rd Euroconference on Foams, Emulsions and their Applications*, Ed. P. L. J. Zitha, J. Banhart, G. L. M. M. Verbist, Verl. MIT, Bremen (2000).
- [25] L. D. Landau, E. M. Lifshitz, *Theory of elasticity*, 3rd edition, Reed, Oxford (1986).
- [26] S. J. Cox, D. Weaire, M. F. Vaz, *Eur. Phys. J. E* **7**, 311 (2002).
- [27] H. M. Princen, *J. Coll. Int. Sci.* **91**, 160 (1983).
- [28] D. R. Lide, *CRC Handbook of Chemistry and Physics*, 84th Ed., CRC Press, Boca Raton (2003).
- [29] H. M. Princen, *J. Coll. Int. Sci.* **105**, 150 (1985).
- [30] I. Cantat, N. Kern, R. Delannay, *Europhys. Lett.* **65**, 726 (2004).
- [31] F. B. Bretherton, *J. Fluid Mech.* **10**, 166 (1961).
- [32] N. D. Denkov, V. Subramanian, D. Gurovich, A. Lips, proceedings of Eufoam 2004, to appear in *Coll. Surf. A* (2004).
- [33] T. Zisis, E. Mitsoulis, *J. Non Newt. Fluid Mech.* **105**, 1 (2002).
- [34] E. Mitsoulis, *Chem. Eng. Sci.* **59**, 789 (2004).
- [35] S. J. Cox, personal communication (2004).
- [36] D. Weaire, S. Hutzler, *Phil. Mag.* **83**, 2747 (2003).
- [37] O. H. Faxén, *Proc. Roy. Swed. Acad. Eng. Sci.* **187**, 1 (1946).
- [38] M. Aubouy, Y. Jiang, J. A. Glazier, F. Graner, *Granular Matt.* **5**, 67 (2003).